Influence of Spin−Orbit Effects on Chemical Reactions: Quantum Scattering Studies for the Cl(^{2}P) + HCl → ClH + Cl(^{2}P) Reaction Using Coupled ab Initio Potential Energy Surfaces[†]

George C. Schatz*

Department of Chemistry, Northwestern University, Evanston, Illinois 60208-3113

Marlies Hankel, T. W. J. Whiteley,[‡] and J. N. L. Connor

Department of Chemistry, University of Manchester, Manchester M13 9PL, U.K.

Received: March 17, 2003; In Final Form: June 13, 2003

We present converged quantum scattering results for the Cl + HCl → ClH + Cl reaction in which the three electronic states that correlate asymptotically to the ground state of Cl(^{2}P) + HCl($^1\Sigma^+$) are included in the dynamical calculations. The potential energy surfaces are taken from recent restricted open-shell coupled-cluster singles doubles with perturbative triples and multireference configuration interaction ab initio computations of A. J. Dobbyn, J. N. L. Connor, N. A. Besley, P. J. Knowles, and G. C. Schatz [*Phys. Chem. Chem. Phys*. **1999**, *1*, 957], as refined by T. W. J. Whiteley, A. J. Dobbyn, J. N. L. Connor, and G. C. Schatz [*Phys. Chem. Chem. Phys*. **2000**, *2*, 549]. The long-range van der Waals portions of the potential surfaces are derived from multisurface empirical potentials due to M.-L. Dubernet and J. M. Hutson [*J. Phys. Chem*. **1994**, *98*, 5844]. Spin−orbit coupling has been included using a spin−orbit parameter that is assumed to be independent of nuclear geometry, and Coriolis interactions are calculated accurately. Reactive scattering calculations have been performed for total angular momentum quantum number $J = {}^1/_2$ using a hyperspherical-coordinate coupled-channel method in full dimensionality. The scattering calculations are used to study the influence of the spin−orbit coupling parameter λ on the fine-structure-resolved cumulative reaction probabilities and transition-state resonance energies with λ varying from −150% to +150% of the true Cl value. The results show the expected dominance of the $^2P_{3/2}$ state to overall reactivity for λ close to the true Cl value and the dominance of the $^2P_{1/2}$ state for λ close to −1 times the true Cl value. Between these two limits, the fine-structure-resolved cumulative reaction probabilities show oscillations as λ varies, statistical behavior being recovered for $\lambda = 0$. We present a two-state model that roughly matches these oscillations and which suggests that the reactivity oscillations are due to coherent mixing of the $\Omega_j = {}^1/_2$ components of the $^2\Sigma$ and $^2\Pi$ states that are derived from the ^{2}P states in the van der Waals regions of the potential surfaces. This mixing leads to inverted spin−orbit propensities (i.e., the upper spin−orbit state is more reactive than the lower one) for certain values of λ. Our analysis of resonance energies indicates significant variation in resonance stability with the value of λ, a general trend being that narrower resonances occur when $|\lambda|$ is smaller than about 50% of the absolute value of the true Cl value, suggesting that narrow resonances occur when there is significant coherent mixing. In addition, we find evidence for Stueckelberg interference oscillations in the total cumulative reaction probabilities due to a conical intersection between the 1 $^2A'$ and 2 $^2A'$ potential surfaces.

I. Introduction

The role of spin−orbit interactions in hydrogen abstraction reactions involving halogen atoms is a topic of both old and new interest in the field of chemical reaction dynamics. It was of interest 30 years ago in studies[1,2] of reactions such as F(^{2}P) + H_2 → FH + H in the context of molecular beam and infrared chemiluminescence experiments. But at that time, the only tractable theory was trajectory surface hopping;[1] in addition, the potential energy surfaces and their couplings were of poor quality. More recently, more sophisticated molecular beam and other experiments[3−5] have stimulated new interest in spin−orbit problems. In addition, it is now possible to apply higher levels of theory than in the past, including quantum scattering calculations with multiple coupled electronic states[6,7] that use more realistic potential functions and couplings.

In the present paper, we will use this newer generation of theory to study spin−orbit effects for the reaction

$$\mathrm{Cl}(^2P) + \mathrm{HCl} \rightarrow \mathrm{ClH} + \mathrm{Cl}(^2P)$$

Our results also apply to other abstraction reactions that are similar to Cl + HCl but have different spin−orbit parameters. In particular, we examine quantum reaction probabilities obtained from multisurface reactive scattering calculations with the goal of understanding how reactivity depends on variations in the spin−orbit coupling. Our interest is to understand, in a general way, why there seems to be a large variation in the behavior of spin−orbit effects for simple hydrogen abstraction reactions.

[†] Part of the special issue "Donald J. Kouri Festschrift".

[‡] Present address: Syrris Ltd., Jarman Way, Royston, Hertfordshire SG8 5HW, U.K.

10.1021/jp034680e CCC: $25.00

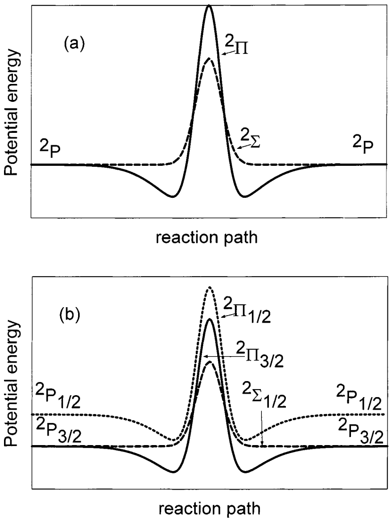

Figure 1. Schematic profiles of the potential surfaces for collinear ClHCl along the reaction path joining reactants and products: (a) nonrelativistic profiles; (b) relativistic profiles, after inclusion of the spin−orbit interaction.

Of most recent interest in this respect has been an experiment by Dong et al.[3] for the $Cl(^2P) + H_2 \rightarrow ClH + H$ reaction, where they found that the excited state, $Cl(^2P_{1/2})$, had larger reactivity than the ground state, $Cl(^2P_{3/2})$, in apparent contradiction to conventional wisdom (and to recent high-level theory[8]) that the excited state should have a higher energy barrier to reaction than the ground state. There has also been renewed interest in the influence of the $^2P_{1/2}$ state for the $F(^2P) + H_2$ reaction,[4] for which it has been found that collisions of $F(^2P_{1/2})$ provide a unique signature on the product-state distributions for sufficiently cold reagents. The experiments of ref 4 have stimulated high-quality theoretical studies[7] in which it has been found that, except for cold reactants, the $F(^2P_{1/2})$ state plays a minor role in determining reactivity. Although the role of atomic $^2P_{1/2}$ states as reactants has only recently been studied in detailed experiments, there is a long history of investigations of spin−orbit branching in reactions that consume or produce halogen atoms, and this has sometimes yielded surprising results in which the excited $^2P_{1/2}$ state was found to be dominant.[9]

Cl + HCl is one of many reactions in which several potential surfaces are asymptotically degenerate (i.e., degenerate in the reagents or products or both) but for which the surfaces split during reaction, providing reaction pathways with different potential energy barriers. The lowest-energy barrier for collinear ClHCl occurs on a surface with $^2\Sigma$ symmetry ($^2A'$ for nonlinear geometries), but the deepest van der Waals well for collinear approach is associated with a surface of $^2\Pi$ symmetry ($^2A'$ and $^2A''$ for nonlinear geometries), which also correlates to the ^2P state of Cl.[10] This is shown schematically in Figure 1a, which illustrates the variation of potential energy along the collinear reaction path. The switch between short- and long-range behavior leads to a crossing between the reactive ($^2\Sigma$) and nonreactive ($^2\Pi$) potential curves about halfway to the top of the $^2\Sigma$ barrier, which provides an opportunity for significant nonadiabatic coupling[6] and Stueckelberg-like interference oscillations (which, curiously, have never been observed for any bimolecular reaction).

Complicating this picture is the presence of spin−orbit coupling, which partially lifts the asymptotic degeneracy (giving the $^2P_{3/2}$ and $^2P_{1/2}$ states of Cl) as shown in Figure 1b. Note that these states are coupled by the electrostatic interaction between Cl and HCl, and the interaction potential is proportional to the difference potential between the $^2\Pi$ and $^2\Sigma$ states.[11] This difference is large and negative in the van der Waals region, while it is large and positive close to the $^2\Sigma$ barrier, so both regions could, in principle, be important for causing transitions between the spin−orbit states while the reactants approach (or the products depart). However the importance of this coupling in controlling the reactivity of different spin−orbit states is not known.

A related issue concerns the influence of the spin−orbit interaction on the energy and stability of transition-state resonances. Such resonances are known for the closely related $I + HI \rightarrow IH + I$ reaction on the basis of photodetachment measurements[12] and reaction dynamics simulations (e.g., ref 13), but there is still uncertainty about their appearance for Cl + HCl, theory showing substantial evidence that they exist (e.g., ref 14) but experiment being less conclusive[15] (see, in addition, ref 16).

There are several levels of sophistication possible when performing nonadiabatic quantum dynamics calculations for reactions with asymptotically degenerate potential surfaces. Here we have chosen a rigorous approach, which uses basis functions in which the electronic orbital and spin angular momenta of the separated reactants and products are explicitly included, along with their coupling to the orbital and rotational angular momenta of the nuclei. It is this approach that we have pursued in our recent work on quantum scattering calculations with multiple surfaces.[6,11,17,18] It leads straightforwardly to the incorporation of electrostatic nonadiabatic, spin−orbit, and Coriolis coupling into the coupled-channel calculations.

The present calculations improve on our earlier studies[6,11,17] in a number of ways, most notably in the use of larger basis sets so that high-energy resonance effects should be more accurately described and in the use of high-quality ab initio potential surfaces and couplings,[19] which have recently been slightly modified to reproduce experimental kinetics data.[18] These surfaces also include long-range potentials[10] (covering the van der Waals wells) the reliability of which has recently been confirmed in ab initio calculations.[20,21] We include spin−orbit effects in the calculations by adding a phenomenological spin−orbit term to the Hamiltonian with a spin−orbit parameter λ that is independent of nuclear geometry. Justification for this assumption is provided by recent relativistic ab initio calculations, which show a shift in the $^2\Sigma$ barrier height due to spin−orbit effects[22] similar to that from the phenomenological spin−orbit term.

In the present paper, we perform scattering calculations for values of the spin−orbit parameter ranging from −150% to +150% of the true value for Cl ($-588\ \text{cm}^{-1}$). This lets us investigate how the dynamics change with λ assuming that the potential surfaces do not vary. In general, positive spin−orbit coupling parameters arise from electrons in an incomplete subshell that is less than half full, whereas negative spin−orbit coupling parameters arise from equivalent electrons in a more than half-filled subshell. We already know[5] that the lowest-energy collinear barrier height (that for the $^2\Sigma$ surface) increases as λ becomes more negative, because the spin−orbit Hamiltonian (for negative λ) preferentially stabilizes the asymptotic $^2P_{3/2}$ state relative to the $^2\Sigma$ barrier, where there is a partial quenching of the spin−orbit effect. Of course, the nature of the potential surfaces is also expected to vary as the spin−orbit constant varies, but here we only consider the latter effect. While varying the spin−orbit parameter is a somewhat artificial procedure, it does allow us to separate the spin−orbit contribution from other sources of nonadiabaticity in the reaction dynamics, thus clarifying the importance of spin−orbit coupling in determining the branching between the fine-structure states. In addition, we find that the role of Stueckelberg interference effects arising from the presence of a conical intersection between the two $^2A'$ symmetry surfaces associated with ClHCl is revealed by this study. Many other atoms have spin−orbit parameters that are in the range that we consider [e.g., F(−265 cm^{-1}), O(−80 cm^{-1}), C(13 cm^{-1}), Na(11.5 cm^{-1}), and K(38.5 cm^{-1})], so the present scattering calculations provide insight into fine-structure effects for other reactions.

Our paper is organized as follows. In section II, we briefly give details of the ab initio potential surfaces, while section III discusses the quantum reactive scattering method. Our results (cumulative reaction probabilities, resonance energies) are presented in section IV, together with a simple two-state dynamical model, which explains some key features in our results. Section V contains our conclusions.

II. Potential Surfaces and Couplings

As mentioned in the Introduction, the potential surfaces employed in our calculations are illustrated qualitatively in Figure 1a for the collinear configuration of the atoms. We use the scaled surfaces of Whiteley et al.[18] collectively denoted sDCBKS, which comprise the following: H_{11}, the "Σ-like" diabatic surface; H_{22}, the "Π-like" diabatic surface; H_{12}, the diabatic coupling surface, and H_{33}, the adiabatic energy of the $^2A''$ surface—it is degenerate with H_{22} at collinearity. The "Σ-like" barrier height in the absence of spin−orbit coupling is 0.37 eV, while the "Π-like" barrier height is 0.77 eV. For collinear geometries, the $^2\Pi$ van der Waals well depth is 0.05 eV, while the $^2\Sigma$ well depth is essentially zero. Note that there is a 0.04 eV deep "Σ-like" well for highly bent geometries, whereas the "Π-like" well disappears for this configuration of the atoms, so the relative importance of the two wells varies with approach geometry.

Figure 1b shows how spin−orbit coupling changes the potential curves of Figure 1a. For the isolated Cl atom, the $^2P_{1/2}$−$^2P_{3/2}$ splitting is 0.109 eV (or 882 cm^{-1}), which is about $^1/_3$ of the $^2\Sigma$ barrier height and twice the $^2\Pi$ van der Waals well depth. The phenomenological spin−orbit Hamiltonian,

$$H_{\rm so} = \lambda \mathbf{L}\cdot\mathbf{S} \tag{1}$$

which reproduces this splitting, has a spin−orbit coupling parameter $\lambda_{\rm Cl}$ equal to −0.073 eV. Because $\lambda_{\rm Cl}$ is negative, the asymptotic energy of the Cl($^2P_{3/2}$) state is lowered relative to Cl($^2P_{1/2}$), and because spin−orbit has little effect on the $^2\Sigma$ potential near the barrier top in Figure 1b, the overall barrier for the $^2\Sigma$ curve is higher (by approximately 33% of the atomic splitting) than it would be in the absence of the spin−orbit interaction. Note that the curves labeled $^2\Sigma_{1/2}$ and $^2\Pi_{3/2}$ in Figure 1b correlate to $^2P_{3/2}$ while $^2\Pi_{1/2}$ correlates to $^2P_{1/2}$. Because of this, one might expect the reaction probability associated with Cl($^2P_{1/2}$) to be much smaller than that for Cl($^2P_{3/2}$). However, additional complications arise when we include the H_{12} electrostatic interaction between the "Σ-like" and the "Π-like" diabats, which gives rise to adiabatic states having 1A′, 2A′, and A″ symmetries. In the presence of spin−orbit coupling, these states have no well-defined spatial or spin symmetry. As a result, the simple reactivity correlations discussed above can be misleading in some situations, as we will see later in section IV.

The sDCBKS potential surfaces and couplings are described in detail in refs 18 and 19, so here we give just a few key features. The short-range potentials are based on restricted open-shell coupled-cluster singles doubles with perturbative triples and multireference configuration interaction levels of theory with a diabatic representation as used by Rebentrost and Lester.[23] The switch to long-range electrostatic potentials[10] occurs near $r_{\rm HCl} = 4.3\ a_0$, independent of $r_{\rm HCl'}$ (note, however, that the potential is invariant to interchanging the two Cls). This switch point is close to the bottom of the barrier to reaction but is inside the van der Waals well. The conical intersection between the "Σ-like" and "Π-like" potentials occurs somewhat inside the switch point, at $r_{\rm HCl} \approx 3.5\ a_0$, $r_{\rm HCl'} \approx 2.5\ a_0$, for geometries along the collinear minimum energy reaction path. The van der Waals minimum occurs at larger distances, at approximately $r_{\rm HCl} = 5.0\ a_0$, $r_{\rm HCl'} = 2.4\ a_0$. For collinear geometries, the saddle point occurs at $r_{\rm HCl} = r_{\rm HCl'} = 2.799\ a_0$ on the $^2\Sigma$ surface and at $r_{\rm HCl} = r_{\rm HCl'} = 2.870\ a_0$ on the $^2\Pi$ surface. Note that for bent geometries a saddle point occurs on the 1^2B_1 surface at an internal angle of 137.4° but for collinear geometries on the $^2\Pi$ surface. However the $^2\Sigma$ barrier for collinear geometries is only 0.062 eV above that for bent (1^2B_1) geometries, so the 1A′ surface is relatively flat as a function of the bend angle.

The long-range parts of the sDCBKS potential surfaces use the empirical potentials of Dubernet and Hutson.[10] The reliability of these long-range empirical potentials has recently been examined by Kłos et al.[20] and Žďánska et al.[21] using ab initio quantum chemical methods. There is generally a good qualitative agreement between the ab initio surfaces and the empirical ones, although there are quantitative differences. Thus for the 1A′ adiabatic surface, the depth of the well for the collinear configuration of the atoms is 383, 438, or 360−370 cm^{-1} according to Dubernet and Hutson,[10] Kłos et al. (their Table 1)[20] or Žďánska et al. [their Figure 3a],[21] respectively. For a T-shaped configuration of the atoms, the well depth on the 1A′ surface is 347, 600 (or 586), or 350−360 cm^{-1} according to Dubernet and Hutson,[10] Kłos et al. (their Table 1 with p 3096 reporting 586 cm^{-1}),[20] or Žďánska et al. [their Figure 3a],[21] respectively. Note that the global minimum for the 1A′ surface is for the collinear configuration according to Dubernet and Hutson[10] and Žďánska et al.[21] but occurs in the T-shaped arrangement on the surface of Kłos et al.[20]

III. Quantum Reactive Scattering Calculations

A. Method. We use the same quantum scattering method that has been employed previously.[11,17] It is similar to an earlier method described by one of us[6] in a preliminary study of Cl + HCl using multiple surfaces. Here we just present sufficient details so that we can introduce notation to indicate the calculations we have done and for our discussion of the results.

We use the notation of Rebentrost and Lester[23] for the four angular momenta involved in the reaction, which is assumed to be of the type

$$A(^2P) + BC \rightarrow AB + C(^2P)$$

where BC and AB are closed-shell ($^1\Sigma$) diatomics. We write the following: $\mathbf{L}$ = electronic orbital angular momentum vector of atom A (or C). L = corresponding quantum number, which has the fixed value $L = 1$ for Cl(^2P). $\mathbf{S}$ = electronic spin angular momentum vector of atom A (or C). S = corresponding quantum number, which has the fixed value $S = {}^1/_2$ for Cl(^2P). $\mathbf{N}$ = nuclear rotational angular momentum of BC (or AB). N = corresponding quantum number, which has the values $N = 0, 1, 2, ...$ $\mathbf{l}$ = nuclear orbital angular momentum of A with respect to BC (or C relative to AB). l = corresponding quantum number, which has the values $l = 0, 1, 2, ...$ We also define the following: $\mathbf{j} = \mathbf{L} + \mathbf{S}$ = electronic total angular momentum; j = corresponding quantum number with values $j = {}^{1}/_{2}$ or $j = {}^{3}/_{2}$. $\mathbf{J} = \mathbf{j} + \mathbf{N} + \mathbf{l}$ = electronic plus nuclear total angular momentum; J = corresponding quantum number with values $J = {}^{1}/_{2}, {}^{3}/_{2}, {}^{5}/_{2}, ...$ (or sometimes $J = {}^{3}/_{2}, {}^{5}/_{2}, {}^{7}/_{2}, ...$).

In addition, we denote by Ω_N, Ω_j, and Ω the body-fixed projection quantum numbers associated with **N**, **j**, and **J**, respectively. The body-fixed z-axis is chosen to lie along the Jacobi vector **R** from the center of mass of the diatom to the atom; we also have $\Omega = \Omega_N + \Omega_j$.

In terms of these quantum numbers, the body-fixed electronic states $|j,\Omega_j\rangle$ are related to the spin and orbital parts of the electronic wave functions by

$$|j,\Omega_j\rangle = \sum_{\Lambda,\Sigma} |L,\Lambda\rangle|S,\Sigma\rangle\langle L,\Lambda,S,\Sigma|j,\Omega_j\rangle \qquad (2)$$

where $\langle l_1,m_1,l_2,m_2|l_3,m_3\rangle$ is a Clebsch−Gordan coefficient. The labels $L = 1$ and $S = {}^{1}/_{2}$ have been omitted from $|j,\Omega_j\rangle$ and the following equations because they have fixed values. In eq 2, $\Lambda = 0, \pm 1$ and $\Sigma = \pm {}^{1}/_{2}$ are the body fixed projection quantum numbers associated with **L** and **S**, respectively. We use the states $|j,\Omega_j\rangle$ to represent the electronic Hamiltonian and as a starting point for the coupled-channel expansion.

We assume that **R** is mass-scaled[24] and define **r** to be the mass-scaled diatom internuclear vector. The Hamiltonian is then given by

$$H = P^2/(2\mu) + \mathbf{l}^2/(2\mu R^2) + p^2/(2\mu) + \mathbf{N}^2/(2\mu r^2) + H_{\mathrm{el}} + H_{\mathrm{so}} \qquad (3)$$

where μ is the scaled reduced mass,[24] P and p are the radial momenta associated with the distances R and r, respectively, H_{el} is the nonrelativistic electronic Hamiltonian, and H_{so} is the spin−orbit Hamiltonian. Mass-polarization terms have been neglected in H_{el} because they should not be important at the low energies that we consider.[23]

In the following treatment, we replace **l** by $\mathbf{J} - \mathbf{j} - \mathbf{N}$ in the centrifugal term in eq 3, which leads to

$$\mathbf{l}^2/(2\mu R^2) = (\mathbf{J}^2 + \mathbf{j}^2 + \mathbf{N}^2)/(2\mu R^2) - (2\mathbf{J}\cdot\mathbf{j} + 2\mathbf{J}\cdot\mathbf{N} - 2\mathbf{N}\cdot\mathbf{j})/(2\mu R^2) \qquad (4)$$

The cross terms in eq 4 produce three types of Coriolis coupling: orbital-electronic, orbital-rotational, and rotational-electronic. All of these terms are evaluated accurately in the coupled-channel calculations described below.

Explicit expressions for H_{el} have been given previously,[11] so we omit them here. The spin−orbit Hamiltonian, H_{so}, is assumed to be given by eq 1 in which the spin−orbit coupling parameter, λ, is taken to be constant, independent of the internuclear distances. The matrix elements of H_{so} are easily evaluated in the $|j,\Omega_j\rangle$ basis set, giving

$$E_{\mathrm{so}}(j) = {}^{1}/_{2}\lambda[j(j + 1) - L(L + 1) - S(S + 1)]$$

along the diagonals of the matrix and zero for all off-diagonal matrix elements. In particular, $E_{\mathrm{so}}(j={}^{3}/_{2}) = \lambda/2$ and $E_{\mathrm{so}}(j={}^{1}/_{2}) = -\lambda$. It is convenient to add $-\lambda/2$ to these energies so that the asymptotic $^2P_{3/2}$ state has zero energy. Other ways of choosing the zero of the energy scale will be considered in section IV, but it should be noted that none of these choices changes the reaction dynamics in any way. In our studies, in which λ is allowed to vary from its experimental Cl value, it is convenient to introduce a scale parameter s defined by

$$s = \lambda/\lambda_{\mathrm{Cl}} \qquad (5)$$

where $\lambda_{\mathrm{Cl}} = -0.073$ eV is the true value for Cl(^2P_j). Note that s is positive when λ is negative and vice versa. Values of s between −1.5 and 1.5 have been considered in our calculations.

B. Coupled-Channel Scattering Calculations. The basis functions used for the coupled-channel calculations are obtained by first combining the electronic states $|j,\Omega_j\rangle$ in eq 2 with angular eigenstates describing the rotational and orbital motion of the nuclei. To do this, we couple the vectors **j** and **N**, to form a resultant vector **F** where $\mathbf{F} = \mathbf{j} + \mathbf{N}$. Note that the resultant z-projection quantum number of **F** along **R** is Ω (the same as the projection of **J**). The resultant electron−nuclear wave functions associated with F and Ω are given by

$$|N,j,F,\Omega\rangle = \sum_{\Omega_j,\Omega_N} |N,\Omega_N\rangle|j,\Omega_j\rangle\langle N,\Omega_N,j,\Omega_j|F,\Omega\rangle \qquad (6)$$

where $|N,\Omega_N\rangle$ is a ket for the rotational state.

Once we have the internal states $|N,j,F,\Omega\rangle$, the coupled-channel expansion for the wave function associated with each partial wave J and space-fixed z-projection quantum number M is given by

$$\Psi^{JM}_{vNjF\Omega} = \sum_{v',N',j',F',\Omega'} D^{J}_{M\Omega'}(\varphi,\theta,0)\Phi_{v'N'}(r)|N',j',F',\Omega'\rangle g^{JvNjF\Omega}_{v'N'j'F'\Omega'}(R) \qquad (7)$$

where $D(\varphi,\theta,0)$ is the rotation matrix that depends on the polar angles φ and θ associated with **R**, the function $\Phi(r)$ is an eigenfunction of the BC rovibrational Hamiltonian, and $g(R)$ is an R-dependent expansion coefficient that is determined numerically by solving a set of coupled Schrödinger equations. In the present case, the Schrödinger equation for the isolated BC molecule is

$$\left[\frac{p^2}{2\mu} + \frac{N(N + 1)\hbar^2}{2\mu r^2} + v(r)\right]\Phi_{vN}(r) = \epsilon_{vN}\Phi_{vN}(r) \qquad (8)$$

where $v(r)$ is the diatomic internuclear potential, v is the vibrational quantum number, and ϵ_{vN} is the rovibrational eigenvalue. Further details of the coupled-channel equations, which are obtained upon substituting eq 7 into the Schrödinger equation, are given in ref 11 along with the transformation of these equations into hyperspherical coordinates so that reactive collisions can be described.

The final result of the calculations is the scattering matrix $\mathbf{S}^J$, which is labeled by the initial and final values of the quantum numbers v, N, j, F, and Ω and an arrangement channel index α. The partial wave cumulative reaction probability $P^J_{\mathrm{cum}}(E)$ (which can be used to calculate rate coefficients) is given by

$$P^J_{\mathrm{cum}}(E) = \sum_{\alpha,v,N,j,F,\Omega} \sum_{\alpha',v',N',j',F',\Omega'} |S^J_{\alpha,v,N,j,F,\Omega\rightarrow\alpha',v',N',j',F',\Omega'}(E)|^2 \qquad (9)$$

where the sums are over all open states at the total energy E and the arrangement channel indices α and α' are chosen to be appropriate for reaction. We also define partial-wave state-selected cumulative probabilities, $P^J_{\mathrm{cum}}(E;j,j')$, that are labeled by the initial and final values of the electronic quantum numbers (j and j'), by restricting the sum in eq 9 appropriately. We then have

$$P^J_{\mathrm{cum}}(E) = \sum_j \sum_{j'} P^J_{\mathrm{cum}}(E;j,j').$$

C. Basis Set and Numerical Parameters. Our multisurface calculations were done using a basis of 342 functions. This basis consists of rotational states $N = 0-13$ for vibrational state $v = 0$, $N = 0-11$ for $v = 1$, and $N = 0-4$ for $v = 2$ in each of the two arrangement channels that are needed for the Cl + HCl reaction. The complete set of ^2P_j electronic states appropriate for $J = {}^1/_2$ was included in all calculations, although only one of the two identical parity components was considered. In earlier work,[18] we examined convergence with respect to basis set size and found that the above basis yields accurate results for the cumulative reaction probabilities for the energy range considered.

Only the $J = {}^1/_2$ partial wave has been included in this study. In earlier work,[18] we converted $J = {}^1/_2$ results into thermal rate coefficients using a J-shifting approximation and made a detailed comparison with experimental rate coefficient data. The validity of the J-shifting approximation for the Cl + HCl reaction has been studied in detail previously.[25] In the present paper, we focus attention on the $J = {}^1/_2$ partial wave cumulative reaction probabilities (both total and j, j' resolved). We hope to study $J > {}^1/_2$ in the future—it will be interesting to see how our conclusions based on the $J = {}^1/_2$ results are modified when higher partial waves are included in the computations.

In earlier research,[18] we have examined rovibrational state-selected cumulative probabilities for $s = 1.0$. Their dependence on s has been calculated as part of the present study; however, we find that $P^J_{\mathrm{cum}}(E)$ and $P^J_{\mathrm{cum}}(E;j,j')$ provide most of the important physical insight that we require. We performed computations for $s = -1.5$, -1.0 to 1.0 (in steps of 0.1), and 1.5 for $E = 0.3-0.7$ eV at intervals of 0.004 or 0.002 eV in the vicinity of resonances. The atomic masses used in the calculations are $m_{\mathrm{H}} = 1.008$ u and $m_{\mathrm{Cl}} = 34.969$ u.

IV. Results

A. Cumulative Reaction Probabilities: Dependence on Total Energy. Figure 2 plots the cumulative probability, $P^J_{\mathrm{cum}}(E)$, for $J = {}^1/_2$ as a function of E from our multisurface calculations, together with the fine-structure state-selected cumulative probabilities, $P^{J=1/2}_{\mathrm{cum}}(E;j,j')$, with the quantum numbers j and j' chosen to be $j = {}^3/_2 \rightarrow j' = {}^3/_2$, $j = {}^1/_2 \rightarrow j' = {}^1/_2$, and $j = {}^3/_2 \rightarrow j' = {}^1/_2$. Note that microscopic reversibility requires $P^{J=1/2}_{\mathrm{cum}}(E;j,j')$ for the $j = {}^1/_2 \rightarrow j' = {}^3/_2$ transition to be equal to that for $j = {}^3/_2 \rightarrow j' = {}^1/_2$ (and we have verified that this is the case to within plotting accuracy), so we only show the latter cumulative probability. Figure 2a displays our results for $s = 1.0$ (i.e., $\lambda = \lambda_{\mathrm{Cl}}$, the true spin−orbit coupling parameter for Cl(^2P_j)), while Figure 2b presents $s = 0.0$, and Figure 2c shows $s = -1.0$. Note that our results in Figure 2a agree with previous results generated with the same basis set and numerical parameters.[18]

The $P^{J=1/2}_{\mathrm{cum}}(E)$ and $j = {}^3/_2 \rightarrow j' = {}^3/_2$ cumulative probabilities in Figure 2a show that the effective reaction threshold (where the cumulative probability first equals 0.1) is near $E = 0.39$ eV. At higher E, there is a gradual rise in the probabilities with a shoulder near $E = 0.45$ eV, a dip at $E = 0.52$ eV, and peaks at $E = 0.54$, 0.60, 0.63, 0.65, and 0.68 eV. The peaks and other structures in Figure 2a reflect contributions from interference and resonance effects that will be studied throughout this paper.

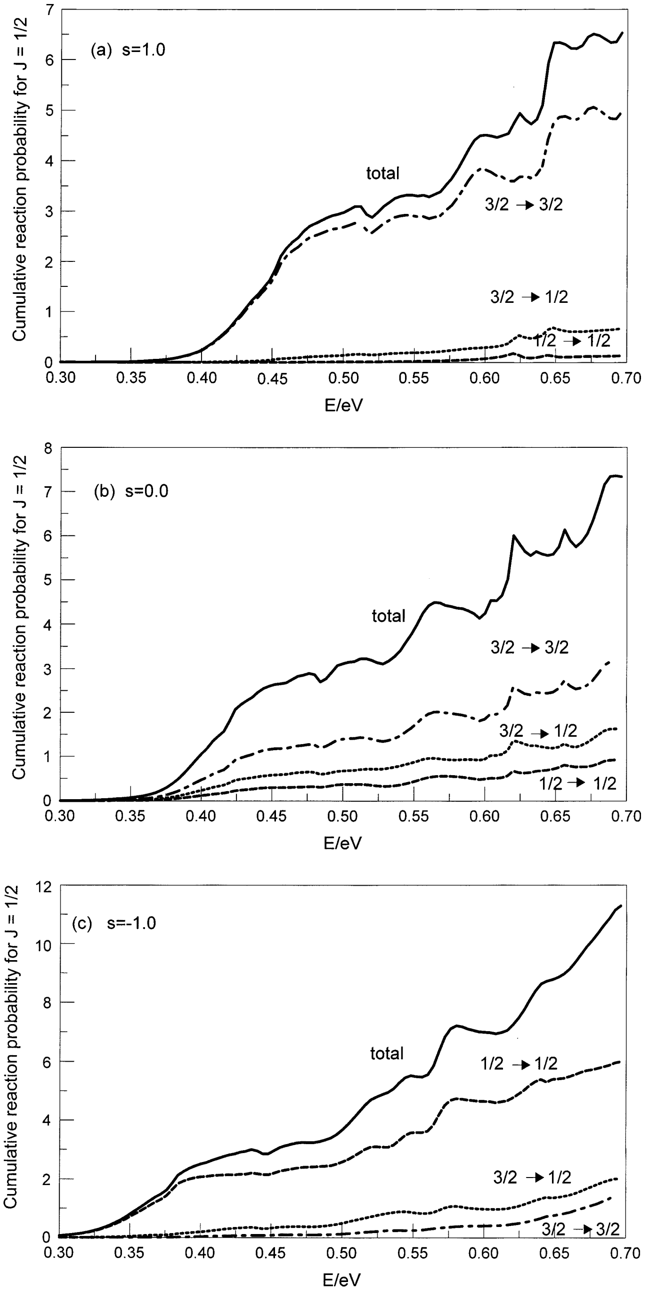

Figure 2. Cumulative reaction probability, $P^{J=1/2}_{\mathrm{cum}}(E)$, and state-selected cumulative reaction probabilities, $P^{J=1/2}_{\mathrm{cum}}(E;j,j')$, versus total energy, E, for $j = {}^3/_2 \rightarrow j' = {}^3/_2$, $j = {}^3/_2 \rightarrow j' = {}^1/_2$, and $j = {}^1/_2 \rightarrow j' = {}^1/_2$: (a) $s = 1.0$; (b) $s = 0.0$; (c) $s = -1.0$. Note that $P^{J=1/2}_{\mathrm{cum}}(E;j,j')$ for $j = {}^3/_2 \rightarrow j' = {}^1/_2$ and $j = {}^1/_2 \rightarrow j' = {}^3/_2$ are identically equal.

The $P^{J=1/2}_{\mathrm{cum}}(E;j,j')$ in Figure 2a for $j = {}^1/_2 \rightarrow j' = {}^1/_2$ and $j = {}^3/_2 \rightarrow j' = {}^1/_2$ are much smaller than the $j = {}^3/_2 \rightarrow j' = {}^3/_2$ cumulative probability, the peaks and dips being less prominent for E below 0.61 eV. The small value of the $j = {}^1/_2 \rightarrow j' = {}^1/_2$ and $j = {}^3/_2 \rightarrow j' = {}^1/_2$ probabilities relative to $j = {}^3/_2 \rightarrow j' = {}^3/_2$ is the expected behavior if the electronic states evolve adiabatically between the reagents and lowest saddle point, because only the $j = {}^3/_2 \rightarrow j' = {}^3/_2$ transition can react by a purely adiabatic route, see Figure 1b.

Our results for $s = -1.0$ in Figure 2c exhibit three important differences compared to Figure 2a. First, we note that the effective threshold energy is much lower at approximately $E = 0.31$ eV rather than $E = 0.39$ eV. Second, we see that the peak

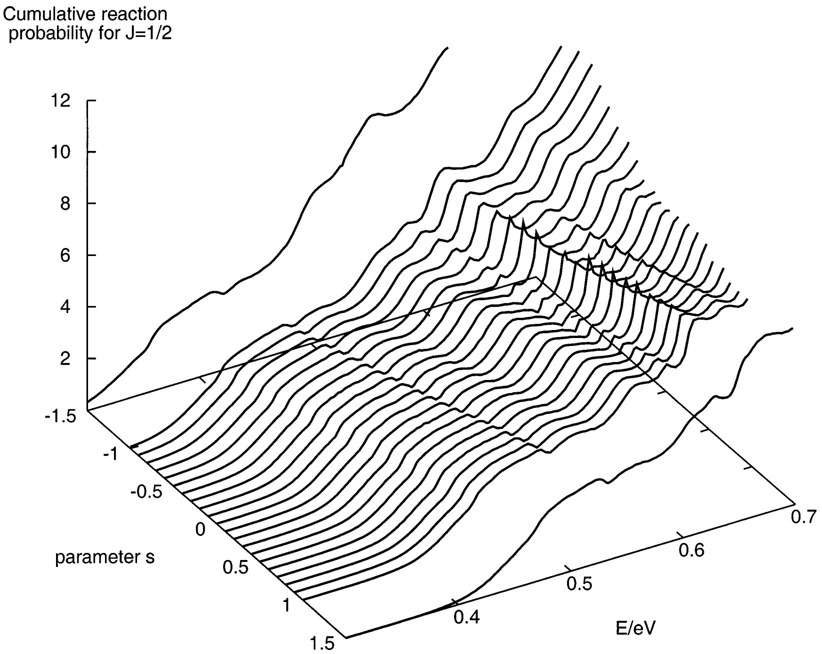

Figure 3. Cumulative reaction probability, $P_{\mathrm{cum}}^{J=1/2}(E)$, versus total energy, E, for $s = -1.5$, -1.0 to 1.0 (in steps of 0.1), and 1.5.

and dip structure is different, the sharp features of Figure 2a being considerably broader in Figure 2c. Third and perhaps most notable, the dominant fine-structure cumulative probability is for $j = {}^{1}/_{2} \rightarrow j' = {}^{1}/_{2}$ rather than for $j = {}^{3}/_{2} \rightarrow j' = {}^{3}/_{2}$.

The $s = 0.0$ cumulative probabilities in Figure 2b have the same oscillatory character as those in Figure 2a,c with sharp peaks at $E = 0.62$ eV and $E = 0.65$ eV. A notable feature of Figure 2b is that the cumulative probabilities are all proportional, the ratio total:$({}^{3}/_{2} \rightarrow {}^{3}/_{2})$:$({}^{3}/_{2} \rightarrow {}^{1}/_{2})$:$({}^{1}/_{2} \rightarrow {}^{1}/_{2})$ being 1:${}^{4}/_{9}$:${}^{2}/_{9}$:${}^{1}/_{9}$ to a good approximation. This is the expected result from statistical theory, in which the 2:1 ratio of $^{2}P_{3/2}$ to $^{2}P_{1/2}$ states for $s = 0.0$ in both reactants and products leads to the observed relative weights for the cumulative probabilities. In particular, the statement in the previous sentence follows upon first noting that the degeneracy, $2j + 1$, of the $j = {}^{1}/_{2}$ and ${}^{3}/_{2}$ states is 2 and 4, respectively. If the states are populated statistically for $s = 0.0$, then their population is ${}^{2}/_{6}$ and ${}^{4}/_{6}$ for $j = {}^{1}/_{2}$ and ${}^{3}/_{2}$, respectively. The statistical reaction probability is then ${}^{4}/_{6} \times {}^{4}/_{6} = {}^{16}/_{36}$ for $j = {}^{3}/_{2} \rightarrow j' = {}^{3}/_{2}$, and ${}^{4}/_{6} \times {}^{2}/_{6} = {}^{8}/_{36}$ for $j = {}^{3}/_{2} \rightarrow j' = {}^{1}/_{2}$ (and for $j = {}^{1}/_{2} \rightarrow j' = {}^{3}/_{2}$) and ${}^{2}/_{6} \times {}^{2}/_{6} = {}^{4}/_{36}$ for $j = {}^{1}/_{2} \rightarrow j' = {}^{1}/_{2}$, which gives rise to the ratios stated above.

Figure 3 displays $P_{\mathrm{cum}}^{J=1/2}(E)$ versus E for 23 values of s in the range -1.5 to 1.5. The plot shows that the peak structures evolve gradually as s changes, which characterizes more completely the relation between Figure 2, panels a, b, and c. Table 1 summarizes the energies of the peaks (and some other structures) for selected values of s. It shows that the energy of each feature generally increases linearly with s with an energy shift of $\Delta E \approx -{}^{1}/_{2}s\lambda_{\mathrm{Cl}} = s \times 0.0365$ eV. This effect is easily rationalized, as previously discussed,[6,11] in terms of the variation of the "Σ-like" barrier height relative to the energy of the $^{2}P_{3/2}$ asymptote. However, note that some of the features sharpen considerably with s (such as the highest-energy peak for s between -0.5 and 0.5), while other features do not.

Figure 4 shows $P_{\mathrm{cum}}^{J=1/2}(E;j,j')$ for the $j = {}^{3}/_{2} \rightarrow j' = {}^{3}/_{2}$ transition as a function of E, for s values in the range -0.5 to 0.5 (in steps of 0.1). Here we see behavior somewhat analogous to Figure 3; however, the fine-structure-resolved probabilities show more complex structures as E changes than does $P_{\mathrm{cum}}^{J=1/2}(E)$. In particular, note that the probabilities do not evolve monotonically with s; instead, there are some spectacular oscillations (for example, Figure 4b shows that the $s = 0.1$ cumulative probability is much smaller than the $s = 0.0$ or $s = 0.2$ probabilities). We will study this finding in greater detail in the next section. The primary point to make for now is that

TABLE 1: Energies (*E*/eV) of Some Prominent Features in $P_{\mathrm{cum}}^{J=1/2}(E)$ for Seven Values of *s*

	feature							
s	shoulder	dip	peak	peak	peak	peak	peak	peak
1.5	0.47	0.54	0.56	0.61	0.63	0.66	0.68	>0.70
1.0	0.45	0.52	0.54	0.59	0.63	0.65	0.68	>0.70
0.5	0.44	0.50	0.53	0.58	0.62	0.64	0.67	>0.70
0.0	0.42	0.49	0.51	0.57	0.60	0.62	0.65	0.69
−0.5	0.40	0.47	0.49	0.54	0.58	0.60	0.63	0.67
−1.0	0.38	0.45	0.47	0.52	0.55	0.57	0.58[a]	0.64
−1.5	0.36	0.42	0.44	0.50	0.53[a]	0.54	0.56[a]	0.62[a]
Ω_N[b]	0, 1	0	1	0	0	1	0	1
saddle point quantum numbers					(0,0,2)	$(0,1^1,2)$	$(0,2^0,2)$	$(0,3^1,2)$

[a] Weak peak, only just visible to graphical accuracy. [b] The Ω_N values indicate the main contributor to $P_{\mathrm{cum}}^{J=1/2}(E)$ from the $P_{\mathrm{cum}}^{J=1/2}(E,\Omega_N,\Omega_N)$ plots in Figure 5.

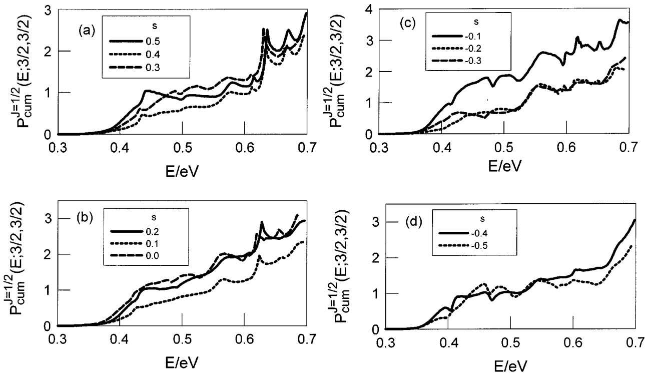

Figure 4. State-selected cumulative reaction probability, $P_{\mathrm{cum}}^{J=1/2}(E;j,j')$, for $j = {}^{3}/_{2} \rightarrow j' = {}^{3}/_{2}$ versus energy, E: (a) $s = 0.5$, 0.4, and 0.3; (b) $s = 0.2$, 0.1, and 0.0; (c) $s = -0.1$, -0.2, and -0.3; (d) $s = -0.4$ and -0.5.

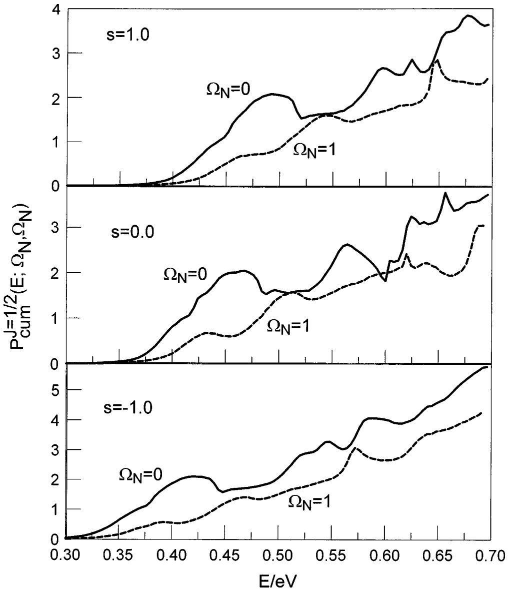

Figure 5. State-selected cumulative reaction probability, $P^{J=1/2}_{\rm cum}(E;\Omega_N,\Omega_N)$, for $\Omega_N = 0$ and $\Omega_N = 1$ versus total energy, E, for $s = 1.0$, 0.0, and -1.0.

there are two levels of oscillatory structure in the cumulative probabilities: that seen in the $P^{J=1/2}_{\rm cum}(E)$ results, as best presented in Figure 3, and that present in the fine-structure-resolved cumulative probabilities, which shows up in Figure 4.

To study the oscillations in $P^{J=1/2}_{\rm cum}(E)$ (in Figure 2), we present in Figure 5 plots of the cumulative reaction probability versus E for $s = 1.0$, 0.0, and -1.0 obtained from eq 9 but with Ω_N and $\Omega_{N'}$, the initial and final rotational projection quantum numbers, respectively, fixed at specified values, that is,

$$P^{J=1/2}_{\rm cum}(E) = \sum_{\Omega_N}\sum_{\Omega_{N'}} P^{J=12}_{\rm cum}(E;\Omega_N,\Omega_{N'})$$

We find that $P^{J=1/2}_{\rm cum}(E;\Omega_N,\Omega_{N'})$ is almost diagonal in Ω_N for each s, so only the dominant diagonal elements have been plotted; in particular, results for $\Omega_N = 0$ and 1 are in Figure 5 ($\Omega_N = 0, \pm1, \pm2$ are allowed). The plots show the expected dominance of $\Omega_N = 0$, corresponding to reactivity on the "Σ-like" surface; however, the $\Omega_N = 1$ cumulative probability is also significant, and moreover, the $\Omega_N = 1$ plots have peaks that alternate with peaks in the $\Omega_N = 0$ curves, at least for E below 0.6 eV. Because the peaks of the $\Omega_N = 0$ and $\Omega_N = 1$ curves occur at different energies, it is possible to label the peak energies in Table 1 according to their Ω_N value. We can see that the peaks (and other structures) have a complex ordering, which suggests that more than one mechanism may be determining their appearance.

One further clue concerning the peaks and structures in Figure 3 comes in Figure 6, in which we have plotted, for $s = 1.0$, the same curves as those in Figure 2a but for a calculation in which the diabatic coupling matrix element V_{12} (between "Σ-like" and "Π-like" states) has been set equal to zero. Note that the spin−orbit states are still coupled by electrostatic interactions in these calculations, and indeed, we see that the $j = {}^3/_2 \rightarrow j' = {}^1/_2$ cumulative probability is about the same as before. However, the primary effect of setting $V_{12} = 0$ is that the conical intersection disappears.

Figure 6 shows that the main effect of this disappearance is to remove the peaks and dips in the curves at low E (below 0.61 eV for $s = 1.0$) but not for high E. This implies a different physical origin for the low E peaks in Figure 3 than for (at least some of) the high E peaks. Indeed, this observation suggests that the low E oscillations in Figure 3 are Stueckelberg-like interference oscillations between the "Π-like" and "Σ-like" amplitudes for reactive scattering, while (at least some of) the higher E oscillations are due to resonances. Thus the lack of structure at low E in Figure 6 would be interpreted as occurring because only one surface has significant amplitude for reaction, that is, "Σ-like" surface.

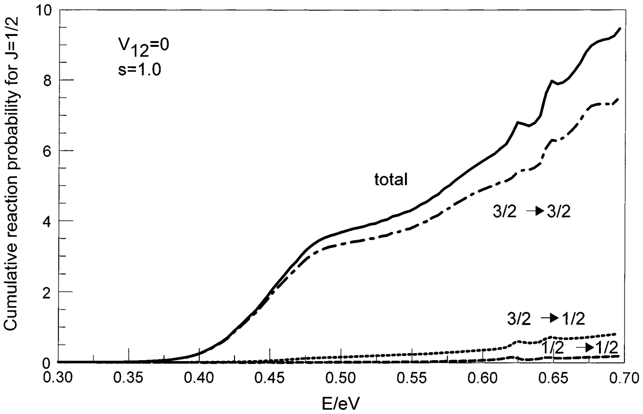

Figure 6. Cumulative reaction probability, $P^{J=1/2}_{\rm cum}(E)$, and state-selected cumulative reaction probabilities, $P^{J=1/2}_{\rm cum}(E;j,j')$, versus total energy, E, for $j = {}^3/_2 \rightarrow j' = {}^3/_2$, $j = {}^3/_2 \rightarrow j' = {}^1/_2$, and $j = {}^1/_2 \rightarrow j' = {}^1/_2$ for $s = 1.0$ with the electrostatic coupling omitted, $V_{12} = 0$. Note that $P^{J=1/2}_{\rm cum}(E;j,j')$ for $j = {}^3/_2 \rightarrow j' = {}^1/_2$ and $j = {}^1/_2 \rightarrow j' = {}^3/_2$ are identically equal.

We also note that the interference oscillations at low E in Figure 3 are approximately independent of s. This makes sense because V_{12} does not depend on s and, as long as we confine our attention to $P^{J=1/2}_{\rm cum}(E)$, any s-dependent interference effects should be averaged out. One further point to note in Figure 6 is that the $V_{12} = 0$ cumulative probability is uniformly larger than that in Figure 2a for $V_{12} \neq 0$. This is consistent with the idea that turning on the conical intersection (i.e., $V_{12} \neq 0$) suppresses reactivity because some component of the "Σ-like" flux is transferred to the nonreactive "Π-like" surface.

B. Cumulative Reaction Probabilities: Dependence on Spin−Orbit Parameter. Next we turn our attention to the variation with s of the $P^{J=1/2}_{\rm cum}(E)$. Figure 7 presents the cumulative probabilities as a function of s at three fixed values of E, Figure 7a referring to $E = 0.4$ eV, Figure 7b to $E = 0.5$ eV, and Figure 7c to $E = 0.6$ eV. Included in the plots is $P^{J=1/2}_{\rm cum}(E)$, as well as the $P^{J=1/2}_{\rm cum}(E;,j,j')$. All three figures show oscillations in the dependence of $P^{J=1/2}_{\rm cum}(E;j,j')$ on s although not, for the most part, in $P^{J=1/2}_{\rm cum}(E)$ vs s. These results are qualitatively similar to what was noticed[11] for an earlier, less accurate surface (denoted sMSGMC[17]), although here we have computed results on a finer grid in s, using a better basis set, so that the behavior of the oscillations is better resolved, and at three energies. There are two adiabatic limits in Figure 7. The first occurs for $s \geq 0.75$, at which the $j = {}^3/_2 \rightarrow j' = {}^3/_2$ transition dominates the reactivity. This can be understood from Figure 1b in terms of an adiabatic motion of the atoms from reactants to products. The second limit occurs for $s \leq -0.6$, where the reactivity receives its dominant contribution from the $j = {}^1/_2 \rightarrow j' = {}^1/_2$ transition. This can also be understood in terms of an adiabatic pathway.

Figure 7 displays remarkable oscillations in the plots of $P^{J=1/2}_{\rm cum}(E;j,j')$ versus s, such that between $s = -0.5$ and 0.5, there are approximately three full oscillations in both the $j = {}^3/_2 \rightarrow j' = {}^3/_2$ and $j = {}^1/_2 \rightarrow j' = {}^1/_2$ cumulative probabilities.

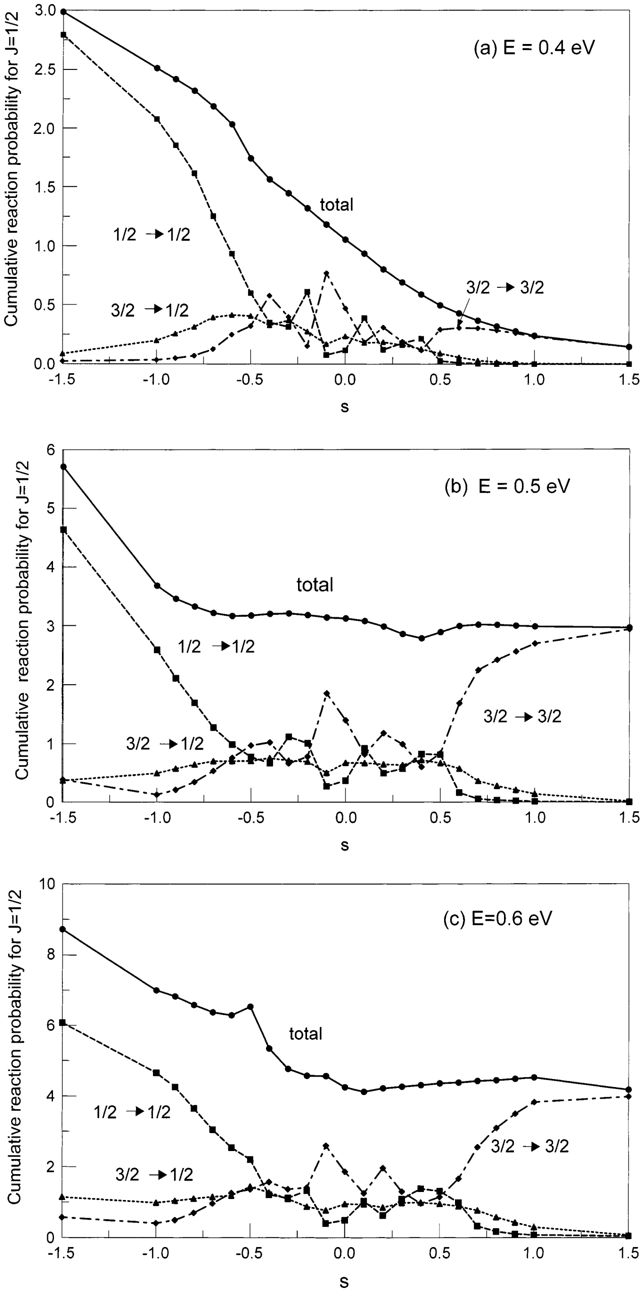

Figure 7. Cumulative reaction probability, $P_{\text{cum}}^{J=1/2}(E)$, and state-selected cumulative reaction probabilities, $P_{\text{cum}}^{J=1/2}(E;j,j')$, versus scaling parameter, s, for $j = {}^3/_2 \rightarrow j' = {}^3/_2$, $j = {}^3/_2 \rightarrow j' = {}^1/_2$, and $j = {}^1/_2 \rightarrow j' = {}^1/_2$: (a) $E = 0.4$ eV; (b) $E = 0.5$ eV; (c) $E = 0.6$ eV. Note that $P_{\text{cum}}^{J=1/2}(E;j,j')$ for $j = {}^3/_2 \rightarrow j' = {}^1/_2$ and $j = {}^1/_2 \rightarrow j' = {}^3/_2$ are identically equal. The solid symbols indicate the s values at which the quantum scattering calculations have been performed.

The $j = {}^3/_2 \rightarrow j' = {}^1/_2$ probability is less sensitive to s. In addition, we see that the $j = {}^3/_2 \rightarrow j' = {}^3/_2$ cumulative probability evolves from being the largest at large s to being smallest at small s with the $s = 0.0$ statistical result noted previously also included. The $j = {}^1/_2 \rightarrow j' = {}^1/_2$ cumulative probability exhibits the reverse behavior as a function of s, while $j = {}^3/_2 \rightarrow j' = {}^1/_2$ is intermediate. In addition, we see that for certain ranges of s, the "wrong" cumulative probability is largest, especially at low E. Thus at $E = 0.4$ eV, the ${}^2P_{1/2}$ state dominates for positive s values near $s = 0.1$ and 0.4, while the ${}^2P_{3/2}$ state dominates for negative s values near $s = -0.1$ and -0.4.

Before we discuss the oscillations in more detail in the next section, there is one point in need of clarification concerning the energy scale used for $P_{\text{cum}}^{J=1/2}(E)$. The choice of the asymptotic ${}^2P_{3/2}$ state for defining the energy zero is somewhat arbitrary, and it is important to realize the consequences of this choice. For clarity, in the remainder of this section, we will use the more explicit notation $E_{j=3/2}$ rather than E.

We have made two other choices for the zero of energy, namely, (a) $s = 0.0$, that is, the weighted mean of the ${}^2P_{3/2}$ and ${}^2P_{1/2}$ energies—we will denote the total energy measured on this scale by $E_{s=0}$—and (b) the lower of the ${}^2P_{3/2}$ and ${}^2P_{1/2}$ energies—we will use the notation E_{lower} for the total energy in this case. The relations between the three energy scales are

$$s \geq 0,\quad \lambda \leq 0 \quad \text{(lower energy state is } {}^2P_{3/2} \text{ because } \lambda_{\text{Cl}} < 0)$$

$$E_{\text{lower}} = E_{j=3/2}$$

$$E_{s=0} = E_{j=3/2} + {}^1/_2\lambda = E_{j=3/2} + {}^1/_2 s\lambda_{\text{Cl}}$$

$$s < 0,\quad \lambda > 0 \quad \text{(lower energy state is } {}^2P_{1/2} \text{ because } \lambda_{\text{Cl}} < 0)$$

$$E_{\text{lower}} = E_{j=3/2} + {}^3/_2\lambda = E_{j=3/2} + {}^3/_2 s\lambda_{\text{Cl}}$$

$$E_{s=0} = E_{j=3/2} + {}^1/_2\lambda = E_{j=3/2} + {}^1/_2 s\lambda_{\text{Cl}}$$

Thus a fixed value for E_{lower} or $E_{s=0}$ for different values of s can be achieved by varying $E_{j=3/2}$ in accordance with the above equation (for $s = -1.0$, the value $E_{\text{lower}} = 0.4$ eV would require $E_{j=3/2} = 0.29$ eV, which is outside the range of our computations, $E_{j=3/2} \in [0.3, 0.7\text{ eV}]$).

Figure 8a shows plots of $P_{\text{cum}}^{J=1/2}(E_{s=0})$ and $P_{\text{cum}}^{J=1/2}(E_{s=0};j,j')$ versus s for $E_{s=0} = 0.4$ eV, while Figure 8b displays $P_{\text{cum}}^{J=1/2}(E_{\text{lower}})$ and $P_{\text{cum}}^{J=1/2}(E_{\text{lower}};j,j')$ versus s for $E_{\text{lower}} = 0.4$ eV. The choice of E_{lower} leads to a sudden switch in energy scale at $s = 0.0$, as is apparent in Figure 8b, the $s = 0.0$ cumulative probability being the largest (because the effective barrier is lowest when there is no spin−orbit coupling). In contrast, the choice of $E_{s=0}$ results in a smoother result in Figure 8a in which the cumulative probability is approximately constant. This can be understood because $E_{s=0}$-(energy of height of effective barrier) is also constant. Of course, our original choice for the zero of the total energy scale is such that the largest $P_{\text{cum}}^{J=1/2}(E_{j=3/2})$ are associated with large negative s, see Figure 7, panels a, b, and c, for $E_{j=3/2} = 0.4$, 0.5, and 0.6 eV, respectively. However, although $P_{\text{cum}}^{J=1/2}(E_{j=3/2})$ varies substantially with s for this choice of energy zero, the oscillations in the fine-structure-resolved probabilities are less affected.

C. Simple Two-State Model for Spin-Orbit Transitions. We discussed the origin of oscillations similar to those in Figure 7 in ref 11, in which we examined the behavior of the Massey parameter governing spin−orbit transitions between the appropriate fine-structure diabats. Here we extend our earlier discussion by presenting a dynamical two-state model for the reaction dynamics, which lets us calculate reaction probabilities that can be compared to our full dimensional results.

In this simple two-state model, we consider the potential along the reaction coordinate for collinear geometries. In this situation, the $\Omega_j = {}^3/_2$ state is uncoupled from the $\Omega_j = {}^1/_2$ state except via Coriolis coupling (details of the argument are given in ref 11), and because the Coriolis coupling mechanism is weak for $J = {}^1/_2$, we ignore it. This means that the only important reactive states (for the parity we choose) at low energy are $j = {}^3/_2$, $\Omega_j = {}^1/_2$ and $j = {}^1/_2$, $\Omega_j = {}^1/_2$ or what in the context of Figure 1 are called ${}^2\Sigma_{1/2}$ (correlating to ${}^2P_{3/2}$) and ${}^2\Pi_{1/2}$ (correlating to ${}^2P_{1/2}$), respectively. The coupling between these two states arises from the "difference potential" for the potential energies of the

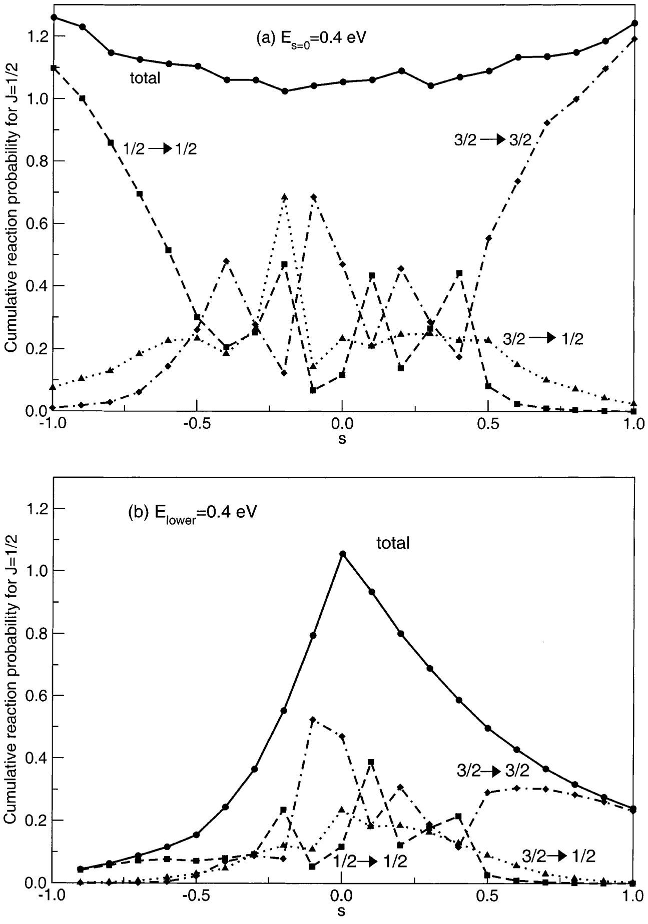

Figure 8. (a) Cumulative reaction probability, $P_{\mathrm{cum}}^{J=1/2}(E_{s=0})$, and state-selected cumulative reaction probabilities, $P_{\mathrm{cum}}^{J=1/2}(E_{s=0};j,j')$ versus scaling parameter, s, for $j = {}^3/_2 \rightarrow j' = {}^3/_2$, $j = {}^3/_2 \rightarrow j' = {}^1/_2$, and $j = {}^1/_2 \rightarrow j' = {}^1/_2$, at $E_{s=0} = 0.4$ eV; (b) Cumulative reaction probability, $P_{\mathrm{cum}}^{J=1/2}(E_{\mathrm{lower}})$, and state-selected cumulative reaction probabilities, $P_{\mathrm{cum}}^{J=1/2}(E_{\mathrm{lower}};j,j')$, versus s at $E_{\mathrm{lower}} = 0.4$ eV. Note that $P_{\mathrm{cum}}^{J=1/2}(E_{s=0};j,j')$ for $j = {}^3/_2 \rightarrow j' = {}^1/_2$ and $j = {}^1/_2 \rightarrow j' = {}^3/_2$ are identically equal and similarly for $P_{\mathrm{cum}}^{J=1/2}(E_{\mathrm{lower}};j,j')$. The solid symbols indicate the s values at which the quantum scattering calculations have been performed.

$^2\Pi_{1/2}$ and the $^2\Sigma_{1/2}$ diabats, $V_\Pi - V_\Sigma$, which we also calculate along the reaction path. Spin–orbit interaction is also included via eq 1, so the asymptotic energies are the same as in the full dimensional calculation, but vibrational and rotational motions are not included.

The two-state Hamiltonian is defined by the matrix

$$\begin{pmatrix} \langle {}^3/_2,{}^1/_2|H_{\mathrm{el}} + H_{\mathrm{so}}|{}^3/_2,{}^1/_2\rangle = {}^2\Sigma_{1/2} & \langle {}^3/_2,{}^1/_2|H_{\mathrm{el}} + H_{\mathrm{so}}|{}^1/_2,{}^1/_2\rangle \\ \langle {}^1/_2,{}^1/_2|H_{\mathrm{el}} + H_{\mathrm{so}}|{}^3/_2,{}^1/_2\rangle & \langle {}^1/_2,{}^1/_2|H_{\mathrm{el}} + H_{\mathrm{so}}|{}^1/_2,{}^1/_2\rangle = {}^2\Pi_{1/2} \end{pmatrix}$$

where the $\langle j',\Omega_{j'}|H_{\mathrm{el}} + H_{\mathrm{so}}|j,\Omega_j\rangle$ matrix elements are given in Table 1 of ref 11, using the quantum numbers $j = {}^3/_2$, $\Omega_j = {}^1/_2$ and $j = {}^1/_2$, $\Omega_j = {}^1/_2$. In Figure 9, we plot the $^2\Sigma_{1/2}$ and $^2\Pi_{1/2}$ diabats (including the spin–orbit interaction for $s = 1.0$ in the diabats), as well as the coupling potential arising from this model, as a function of the reaction path. It is important to realize that the curves in Figure 9 are functions of a single coordinate in our simple two-state model and are approximations to the full $\langle j',\Omega_{j'}|H_{\mathrm{el}} + H_{\mathrm{so}}|j,\Omega_j\rangle$ matrix elements, which are functions of two independent coordinates for the collinear configuration of the atoms. Note that the $^2\Pi_{1/2}$ curve in Figure 9 has the deeper van der Waals well and higher barrier, so it would cross the $^2\Sigma_{1/2}$ curve if the energy shift arising from the spin–orbit interaction was omitted.

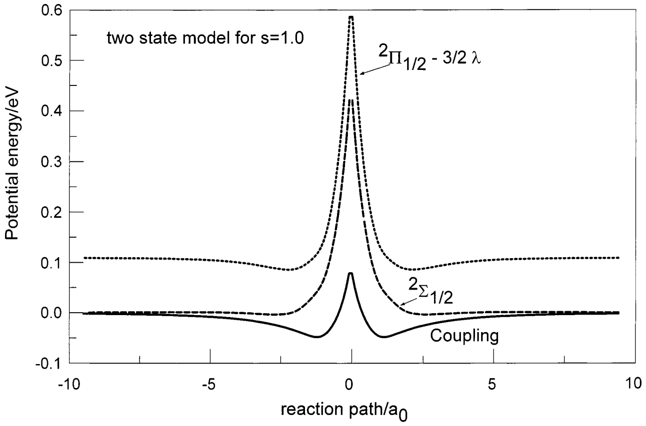

Figure 9. Two-state model potential energies and coupling. The diabats $^2\Sigma_{1/2}$ and $^2\Pi_{1/2} - {}^3/_2\lambda$ include the spin–orbit interaction for $s = 1.0$.

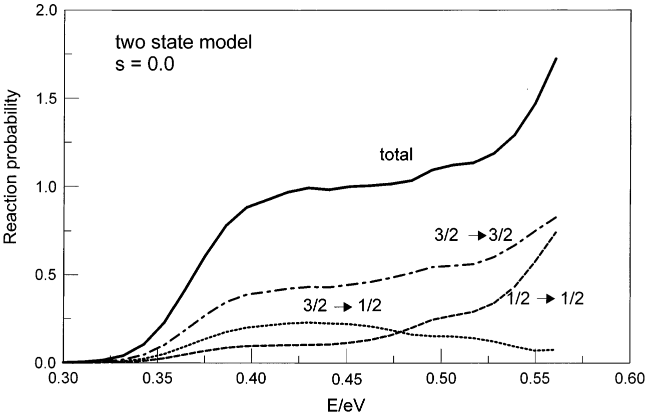

Figure 10. Two-state model reaction probabilities versus total energy, E, for $j = {}^3/_2 \rightarrow j' = {}^3/_2$, $j = {}^3/_2 \rightarrow j' = {}^1/_2$, and $j = {}^1/_2 \rightarrow j' = {}^1/_2$ at $s = 0.0$. Note that the reaction probabilities for $j = {}^3/_2 \rightarrow j' = {}^1/_2$ and $j = {}^1/_2 \rightarrow j' = {}^3/_2$ are identically equal.

We have solved the Schrödinger equation for this two-state model to determine the fine-structure and total reaction probabilities as a function of the total energy E and the scaling parameter s. As before, E is always measured with respect to the asymptotic $^2\Sigma_{1/2}$ energy (energy of the $^2P_{3/2}$ state).

Figure 10 shows, for $s = 0.0$, the spin–orbit reaction probabilities plotted versus E. This figure is to be compared with Figure 2b for the full dynamics, and indeed, there is much similarity. The simple model does not incorporate vibrational zero-point energy, so the reactive threshold is lower. Note that there are weak shoulders in the total reaction probability in Figure 10 at $E = 0.4$ and 0.5 eV. This is similar to the broad peaks seen in the middle panel of Figure 5, which we indicated could be due to interference oscillations. Of course in the single-coordinate model, the intersection of the $^2\Sigma_{1/2}$ and $^2\Pi_{1/2}$ curves is not conical, and we do not expect exact agreement.

Figure 11 shows fine-structure and total reaction probabilities versus s at fixed E (choosing $E = 0.35$ eV). This energy yields graphs that are similar to Figure 7a, both for the total reaction probability and for the fine-structure-resolved probabilities. In particular, there are oscillations for $-0.5 < s < 0.5$ that are similar to what we see in Figure 7a, with the $j = {}^3/_2 \rightarrow j' = {}^3/_2$ and $j = {}^1/_2 \rightarrow j' = {}^1/_2$ transitions influenced much more strongly than the $j = {}^3/_2 \rightarrow j' = {}^1/_2$ transition. However, there is only one distinct oscillation in Figure 11, whereas there are three in Figure 7a. This suggests that our simple two-state model captures the essence of the phenomenon responsible for the oscillations, although the agreement is only qualitative.

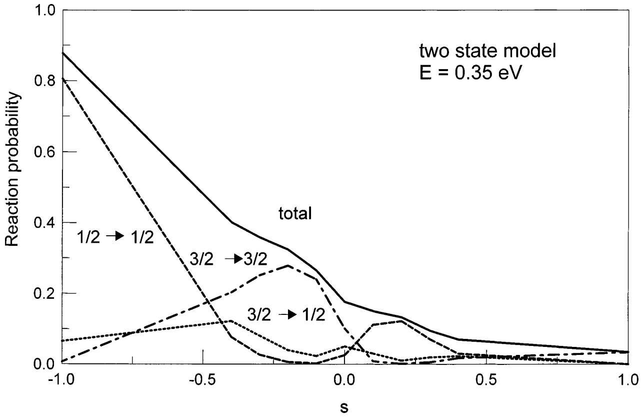

Figure 11. Two-state model reaction probabilities versus s for $j = {}^3/_2 \rightarrow j' = {}^3/_2$, $j = {}^3/_2 \rightarrow j' = {}^1/_2$, and $j = {}^1/_2 \rightarrow j' = {}^1/_2$ at $E = 0.35$ eV. Note that the reaction probabilities for $j = {}^3/_2 \rightarrow j' = {}^1/_2$ and $j = {}^1/_2 \rightarrow j' = {}^3/_2$ are identically equal.

If we now reexamine the potential curves in Figure 9, we see that the coupling between the diabats is large in magnitude in three regions: (1) in the reactant region, where the $^2\Pi_{1/2}$ curve has its van der Waals well, (2) in the corresponding product region, and (3) close to the barrier maxima. Figure 9 is for $s = 1.0$, but the coupling potential remains the same for smaller $|s|$, although the diabats are then closer together and there is a greater probability of hopping. The oscillations as a function of s can then be understood in terms of the amount of cycling of populations between the two diabats that occurs during the reaction. For large $|s|$, the hopping probability is small and the results are largely adiabatic. For $|s| < 0.5$, there is sufficient hopping that the populations cycle between the two diabats, and the populations then oscillate as a function of s. This effect shows up primarily in the $j = {}^3/_2 \rightarrow j' = {}^3/_2$ and $j = {}^1/_2 \rightarrow j' = {}^1/_2$ reaction probabilities. The total reaction probability is the sum over different final outcomes and thus is less sensitive to the amount of cycling that occurs.

This explanation confirms an earlier analysis in ref 11, in which we demonstrated that the variation of the Massey parameter was consistent with a strong cycling of populations for $|s| < 0.5$. Now we have shown that a two-state reaction path model leads to oscillations in the reaction probabilities as a function of s. Of course, there will also be oscillations as a function of E, and this is one reason the fine-structure-resolved cumulative probabilities in Figure 4 show more structure as a function of E than do the total cumulative probabilities in Figure 3.

To conclude this section, we mention that there is a second simple two-state model that may be used to understand the branching between the $^2P_{1/2}$ and $^2P_{3/2}$ states for $s \approx 0.0$. It is a unitary transformation of the one we have just analyzed. In this second model, we use the $|\Lambda,\Sigma\rangle \equiv |L,\Lambda\rangle|S,\Sigma\rangle$ basis functions of eq 2 with $L = 1$, $S = {}^1/_2$ rather than the $|j,\Omega_j\rangle$ functions. Thus for $\Omega = {}^1/_2$, the two basis functions are $|1,-{}^1/_2\rangle$ for $\Lambda = 1$, $\Sigma = -{}^1/_2$ and $|0,{}^1/_2\rangle$ for $\Lambda = 0$, $\Sigma = {}^1/_2$. In this basis set, the electrostatic Hamiltonian is diagonal asymptotically, and the spin−orbit interaction causes the states to be coupled. We find from eq 2 that the two asymptotic states are

$$|j={}^1/_2,\Omega_j={}^1/_2\rangle = -(1/\sqrt{3})|0,{}^1/_2\rangle + \sqrt{{}^2/_3}|1,-{}^1/_2\rangle$$
$$= -0.58|0,{}^1/_2\rangle + 0.82|1,-{}^1/_2\rangle$$

for $^2P_{1/2}$ and

$$|j={}^3/_2,\Omega_j={}^1/_2\rangle = \sqrt{{}^2/_3}|0,{}^1/_2\rangle + (1/\sqrt{3})|1,-{}^1/_2\rangle$$
$$= 0.82|0,{}^1/_2\rangle + 0.58|1,-{}^1/_2\rangle$$

for $^2P_{3/2}$. From these equations, we can see the relative participation of the $^2\Sigma_{1/2}$, that is, $|0,{}^1/_2\rangle$, and $^2\Pi_{1/2}$, that is, $|1,-{}^1/_2\rangle$, states in the correct asymptotic states. This then suggests a sudden approximation, in which we imagine that the dynamics is either completely "$^2\Sigma_{1/2}$-like" or completely "$^2\Pi_{1/2}$-like", reaction associated with the $^2P_{1/2}$ and $^2P_{3/2}$ states being determined only by the state mixings just given. In other words, we assume there is a scattering matrix element for the $j = {}^3/_2 \rightarrow j' = {}^3/_2$ transition that is given by

$$\langle j={}^3/_2|S|j'={}^3/_2\rangle =$$
$$[0.82\langle 0,{}^1/_2| + 0.58\langle 1,-{}^1/_2|]S[0.82|0,{}^1/_2\rangle + 0.58|1,-{}^1/_2\rangle]$$
$$= 0.67\langle 0,{}^1/_2|S|0,{}^1/_2\rangle + 0.34\langle 1,-{}^1/_2|S|1,-{}^1/_2\rangle$$
$$\approx 0.67S_\Sigma$$

where in the last line we have assumed that reaction only occurs on the $^2\Sigma_{1/2}$ surface.

We can apply this argument again to calculate all of the reaction probabilities, obtaining

$$P(j={}^3/_2\rightarrow j={}^3/_2) = 0.67^2P_\Sigma = 0.45P_\Sigma$$

$$P(j={}^3/_2\rightarrow j'={}^1/_2) = 0.48^2P_\Sigma = 0.23P_\Sigma$$

$$P(j={}^1/_2\rightarrow j'={}^1/_2) = 0.34^2P_\Sigma = 0.11P_\Sigma$$

where $P_\Sigma = |S_\Sigma|^2$ is the $^2\Sigma_{1/2}$ reaction probability. This argument predicts that the three probabilities for $s \approx 0.0$ should be in the order 0.45, 0.23, 0.11, which is indeed the order that we find in Figure 10 for $E = 0.4$ eV at which the exact two-state reaction probabilities are 0.39, 0.20, and 0.10, respectively. However the sudden approximation is evidently a drastic oversimplification when $s \approx 1.0$, and we find that it exaggerates the smaller reaction probabilities (the calculated two-state reaction probabilities at $E = 0.4$ eV for $s = 1.0$ are 0.56, 0.02, and 0.01). Note that the sudden approximation does not predict oscillations as a function of s. However oscillations could occur if we included both the $^2\Sigma_{1/2}$ and $^2\Pi_{1/2}$ scattering amplitudes, resulting in interference between the two reactive pathways.

D. Transition-State Resonances. Next we consider the sharp structures in Figures 2 and 3. Past (single-surface) studies[26] of ClHCl based on the BCMR surface[27] have observed one resonance feature over the energy range considered, namely, a peak near $E = 0.642$ eV with a full width at half-maximum of about 0.004 eV. This resonance was assigned the saddle-point quantum numbers (ν_1,ν_2,ν_3) = (symmetric stretch, bend, asymmetric stretch) = (0,0,2) on the basis of the appearance of the scattering wave function close to the saddle point. A similar resonance is seen[27] in exact quantum computations for collinear ClHCl; there are also resonances at higher energies that correspond to higher excitations of the ν_3 mode, but lower-energy resonances, such as those for the state (0,0,0), are not sufficiently stable to show narrow structure.

Figure 3 exhibits eight structures that might be interpreted as being resonances, which we have tabulated in Table 1 for seven values of $s = -1.5$ to 1.5 (steps of 0.5). However, our analysis in sections IV.A and IV.B, particularly the effect of setting the diabatic coupling between the "Σ-like" and "Π-like" surfaces, $V_{12} = 0$, in Figure 6, lets us identify three of these structures as arising from interference effects rather than being single-surface resonances (the lowest-energy structure is a shoulder). Of course, resonances could appear as a result of the conical intersection (so-called funnel resonances); however, the shape of the conical intersection in Cl + HCl is not expected to be favorable for such resonances.

The higher-energy peaks (above $E = 0.60$ eV for $s = 1.0$) show up consistently in calculations both with and without the electrostatic coupling, V_{12}, included, so it is easier to assign these peaks. In Table 1, we assigned saddle-point quantum numbers, giving the lowest-energy resonance the same quantum numbers as previously inferred from single-surface calculations[18] (with corrections for the spin−orbit induced shift of the effective barrier height). Thus for $s = 1.0$, the (0,0,2) resonance is at $E = 0.63$ eV.

We also find a resonance only 0.02 eV higher in energy than the (0,0,2) one for $s = 1.0$. Using the $\Omega_N = \Omega_{N'}$ assignments in Figure 5, we find that it corresponds to the first excited bend state built out of (0,0,2), namely, $(0,1^1,2)$ because $\Omega_N = \Omega_{N'} = 1$ corresponds to one quantum of vibrational angular momentum at the saddle point for the first excited bend state. Appropriately, this resonance is missing in the $J = 0$ single-surface results that were reported in ref 18 (which should only show $\Omega_N = \Omega_{N'} = 0$ resonances). The next peak at $E = 0.68$ eV for $s = 1.0$ can then be assigned as a second excited bend resonance, presumably with the quantum numbers $(0,2^0,2)$ because we see it in the $\Omega_N = \Omega_{N'} = 0$ results in Figure 5, and a peak at $E = 0.71$ eV for $s = 1.0$ can be identified as $(0,3^1,2)$ on the basis of its appearance in the $\Omega_N = \Omega_{N'} = 1$ results in Figure 5.

By allowing s to vary away from $s = 1.0$, we can then assign the other resonances in Table 1 when $s \neq 1.0$. Figure 3 shows the evolution of these resonances as a function of s, and we see that for $|s| < 0.5$ they are sharper than those for $s > |0.5|$. This may be due to the interference effects discussed in section IV.C; however, this tentative explanation requires further investigation.

V. Conclusions

This paper has examined the influence of spin−orbit coupling on reactions of open-shell atoms with closed-shell diatomic molecules, which we have modeled by the Cl + HCl → ClH + Cl reaction. We find that electrostatic coupling between the spin−orbit states leads to a variety of interference phenomena that modify the reaction dynamics compared with reaction on a single potential surface.

Our primary tool for this study has been quantum reactive scattering calculations for $J = {}^1/_2$ in which we varied the spin−orbit parameter over the range −150% to +150% of its correct value. In this way, we demonstrated that the $P_{\rm cum}^{J=1/2}(E;j,j')$ values undergo a change from adiabatic character for large positive and large negative values of λ to statistical behavior for $\lambda = 0$ with coherent oscillations between the adiabatic and statistical limits. This leads to a range of λ values for which "inverted" behavior is observed in the cumulative reaction probabilities, which means that the excited spin−orbit state has larger reactivity than the ground state.

We introduced a simple two-state model for the reaction dynamics that mimics some features of the full dynamics quite well. It demonstrated that the coupling between the $^2\Sigma_{1/2}$ and $^2\Pi_{1/2}$ states along the collinear reaction path in the van der Waals well region noticeably influences the $j \rightarrow j'$ resolved reaction propensities.

We also found evidence for the existence of Stueckelberg-type interference oscillations in plots of $P_{\rm cum}^{J=1/2}(E)$ versus E that arise from a conical intersection between the potential surfaces about halfway to the top of the $^2\Sigma_{1/2}$ potential barrier. Finally we examined the properties of transition-state resonances associated with ClHCl. We found that spin−orbit coupling between the surfaces broadens the resonances in the adiabatic regime but sharpens them in the coherent coupling regime.

The connection between the present results and experiment will be an important task for future research. The small spin−orbit effects that we find when the true value of λ for Cl is used (i.e., $\lambda = \lambda_{\rm Cl}$) have often been observed[9] in reactions of $\rm Cl(^2P_j)$, but it will be of more interest to find reactions that exhibit the more dramatic spin−orbit effects that we have predicted. Our results indicate that the magnitude of the spin−orbit interaction relative to the van der Waals well depth is an important parameter for determining whether interesting spin−orbit propensities are possible. A useful aspect of our simple two-state model is that it is easily applied to a variety of reactions, which should make it possible to identify candidates for further study.

Acknowledgment. This research was supported by the U.S. National Science Foundation (Grant No. CHE-0131998) and the U.K. Engineering and Physical Sciences Research Council.

References and Notes

(1) Tully, J. C. *J. Chem. Phys.* **1974**, *60*, 3042.

(2) Jaffe, R. L.; Morokuma, K.; George, T. E. *J. Chem. Phys.* **1975**, *63*, 3417.

(3) Dong, F.; Lee, S.-H.; Liu, K. *J. Chem. Phys.* **2001**, *115*, 1197. Lee, S.-H.; Liu, K. *J. Chem. Phys.* **1999**, *111*, 6253. Lee, S.-H.; Lai, L.-H.; Liu, K.; Chang, H. *J Chem. Phys.* **1999**, *110*, 8229. Liu, K. *Annu. Rev. Phys. Chem.* **2001**, *52*, 139. Liu, K. *Int. Rev. Phys. Chem.* **2001**, *20*, 189.

(4) Harper, W. W.; Nizkorokov, S. A.; Nesbitt, D. J. *J. Chem. Phys.* **2002**, *116*, 5622. Nizkorodov, S. A.; Harper, W. W.; Nesbitt, D. J. *Faraday Discuss.* **1999**, *113*, 107. Nizkorodov, S. A.; Harper, W. W.; Chapman, W. B.; Blackmon, B. W.; Nesbitt, D. J. J. *Chem. Phys.* **1999**, *111*, 8404.

(5) Ausfelder, F.; Kelso, H.; McKendrick, K. G. *Phys. Chem. Chem. Phys.* **2002**, *4*, 473. Ausfelder, F.; McKendrick, K. G. *Prog. React. Kinet. Mech.* **2000**, *25*, 299. Sweeney, G. M.; McKendrick, K. G. *J. Chem. Phys.* **1997**, *106*, 9182. Sweeney, G. M.; Watson, A.; McKendrick, K. G. *J. Chem. Phys.* **1997**, *106*, 9172. Brouard, M.; O'Keeffe, P.; Vallance, C. *J. Phys. Chem. A* **2002**, *106*, 3629. Brouard, M.; Vallance, C. *Phys. Chem. Chem. Phys.* **2001**, *3*, 3602. Matsumi, Y.; Izumi, K.; Skorokhodov, V.; Kawasaki, M.; Tanaka, N. *J. Phys. Chem. A* **1997**, *101*, 1216. Tyndall, G. S.; Orlando, J. J.; Kegley-Owen, C. S. *J. Chem. Soc., Faraday Trans.* **1995**, *91*, 3055. Chichinin, A. I. *Khim. Fiz.* **2000**, *19* (3), 127. Chichinin, A. I. *J. Chem Phys.* **2000**, *112*, 3772. Chichinin, A. I. *Khim. Fiz.* **1997**, *16* (4), 57 [English translation. *Chem. Phys. Rep.* **1997**, *16*, 635]. Chichinin, A. I. *Khim. Fiz.* **1996**, *15* (6), 49 [English translation. *Chem. Phys. Rep.* **1996**, *15*, 843].

(6) Schatz, G. C. *J. Phys. Chem.* **1995**, *99*, 7522. In eq 2, for "+2**N·j**" read "−2**N·j**". In eq 7, for "P^{2}" read "p^{2}". In Table 1, for "v_{00}, v_{20}" read "V_{00}, V_{20}". In section IV, for "λ" read "$|\lambda|$". In the caption to Figure 3, for "ref 24", read "ref 25". In ref 25, for "*91*, 5496", read "*93*, 251".

(7) Alexander, M. H.; Werner, H.-J.; Manolopoulos, D. E. *J. Chem. Phys.* **1998**, *109*, 5710. Alexander, M. H.; Manolopoulos, D. E.; Werner, H.-J. *J. Chem. Phys.* **2000**, *113*, 11084. Aoiz, F. J.; Bañares, L.; Castillo, J. F. *J. Chem. Phys.* **1999**, *111*, 4013. Aquilanti, V.; Cavalli, S.; De Fazio, D.; Volpi, A.; Aguilar, A.; Giménez, X.; Lucas, J. M. *Phys. Chem. Chem. Phys.* **2002**, *4*, 401. Honvault, P.; Launay, J.-M. *Chem. Phys. Lett.* **1999**, *303*, 657. Aquilanti, V.; Cavalli, S.; De Fazio, D.; Volpi, A. *Int. J. Quantum Chem.* **2001**, *85*, 368. Aquilanti, V.; Cavalli, S.; Pirani, F.; Volpi, A.; Cappelletti, C. *J. Phys. Chem. A* **2001**, *105*, 2401.

(8) Alexander, M. H.; Capecchi, G.; Werner, H.-J. *Science* **2002**, *296*, 715.

(9) Husain, D.; Donovan, R. J. *Adv. Photochem.* **1970**, *8*, 1. Donovan, R. J.; Husain, D. *Chem. Rev.* **1970**, *70*, 489. Dagdigian, P. J.; Campbell, M. L. *Chem. Rev.* **1987**, *87*, 1. Dagdigian, P. J. In *Selectivity in Chemical Reactions*; Proceedings of the NATO Advanced Research Workshop, Bowness-on-Windermere, U.K., 7−11 September 1987; Whitehead, J. C., Ed.; Kluwer: Dordrecht, Netherlands, 1988; pp 147−177. González-Ureña, A.; Vetter, R. *J. Chem. Soc., Faraday Trans.* **1995**, *91*, 389. Alagia, M.; Balucani, N.; Casavecchia, P.; Stranges, D.; Volpi, G. G. *J. Chem. Soc., Faraday Trans.* **1995**, *91*, 575.

(10) Dubernet, M.-L.; Hutson, J. M. *J. Phys. Chem*. **1994**, *98*, 5844.

(11) Schatz, G. C.; McCabe, P.; Connor, J. N. L. *Faraday Discuss*. **1998**, *110*, 139.

(12) Weaver, A.; Metz, R. B.; Bradforth, S. E.; Neumark, D. M. *J. Phys. Chem*. **1988**, *92*, 5558. Waller, I. M.; Kitsopoulos, T. N.; Neumark, D. M. *J. Phys. Chem*. **1990**, *94*, 2240. Liu, Z.; Gómez, H.; Neumark, D. M. *Faraday Discuss*. **2001**, *118*, 221.

(13) Manz, J.; Römelt, J. *Chem. Phys. Lett*. **1981**, *81*, 179. Schatz, G. C. *J. Chem. Phys*. **1989**, *90*, 4847. Schatz, G. C. *J. Phys. Chem*. **1990**, *94*, 6157. Schatz, G. C.; Sokolovski, D.; Connor, J. N. L. *Faraday Discuss. Chem. Soc*. **1991**, *91*, 17. Noli, C.; Connor, J. N. L.; Rougeau, N.; Kubach, C. *Phys. Chem. Chem. Phys*. **2001**, *3*, 3946. Noli, C.; Connor, J. N. L. *Russ. J. Phys. Chem*. **2001**, *76* (Suppl. 1), S77; physics/0301054.

(14) Schatz, G. C. *J. Phys. Chem*. **1990**, *94*, 6157.

(15) Metz, R. B.; Weaver, A.; Bradforth, S. E.; Kitsopoulos, T. N.; Neumark, D. M. *J. Phys. Chem*. **1990**, *94*, 1377. Metz, R. B.; Kitsopoulos, T. N.; Weaver, A.; Neumark, D. M. *J. Chem. Phys*. **1988**, *88*, 1463.

(16) Liu, K.; Kolessov, A.; Partin, J. W.; Bezel, I.; Wittig, C. *Chem. Phys. Lett*. **1999**, *299*, 374. Imura, K.; Ohoyama, H.; Naaman, R.; Che, D.-C.; Hashinokuchi, M.; Kasai, T. *J. Mol. Struct*. **2000**, *552*, 137. Che, D.-C.; Hashinokuchi, M.; Shimizu, Y.; Ohoyama, H.; Kasai, T. *Phys. Chem. Chem. Phys*. **2001**, *3*, 4979.

(17) Maierle, C. S.; Schatz, G. C.; Gordon, M. S.; McCabe, P.; Connor, J. N. L. *J. Chem. Soc., Faraday Trans*. **1997**, *93*, 709.

(18) Whiteley, T. W. J.; Dobbyn, A. J.; Connor, J. N. L.; Schatz, G. C. *Phys. Chem. Chem. Phys*. **2000**, *2*, 549. On p 549, for "$\mathrm{C}_{\mathrm{cov}}$" read "$\mathrm{C}_{\infty\mathrm{v}}$"; on p 551, for "$\boldsymbol{I}$" read "$\boldsymbol{l}$"; on p 553, for "$\mathrm{V}_{21} = 0$" read "$\mathrm{V}_{12} \neq 0$"; in Table 3, for "$15^{-17}$" read "$10^{-15}$" and for "9.8" read "9.48"; on p 554, for "$\Omega_N{}^{1/2}$" read "$\Omega_{N'}$"; in ref 44, for "Zang" read "Zhang".

(19) Dobbyn, A. J.; Connor, J. N. L.; Besley, N. A.; Knowles, P. J.; Schatz, G. C. *Phys. Chem. Chem. Phys*. **1999**, *1*, 957. On p 712, for "$\gamma = 152°$" read "$\theta = 152°$"; in Figures 4c and 4(d), for "ClCHI" read "ClHCl"; in eq 6, for "$+2\mathbf{N}\cdot\mathbf{j}$" read "$-2\mathbf{N}\cdot\mathbf{j}$"; in eq 11, for "$\mathrm{P}^2$" read "$\mathrm{p}^2$"; below eq 11, for "Substitution of eq 1" read "Substitution of eq 10"; in Figure 6, for "$P^{J}_{\mathrm{cum}}(E;_{1}1/2,1/2)$" read "$P^{J}_{\mathrm{cum}}(E;1/2,1/2)$".

(20) Kłos, J. A.; Chałasiński, G.; Szczęśniak, M. M.; Werner, H.-J. *J. Chem. Phys*. **2001**, *115*, 3085.

(21) Žďánska, P.; Nachtigallová, D.; Nachtigall, P.; Jungwirth, P. *J. Chem. Phys*. **2001**, *115*, 5974.

(22) Visscher, L.; Dyall, K. G. *Chem. Phys. Lett*. **1995**, *239*, 181.

(23) Rebentrost, F.; Lester, W. A., Jr. *J. Chem. Phys*. **1975**, *63*, 3737; **1976**, *64*, 3879; **1976**, *64*, 4223; **1977**, *67*, 3367. Rebentrost, F. In *Theoretical Chemistry*: *Advances and Perspectives, Theory of Scattering*: *Papers in Honor of Henry Eyring*; Henderson, D., Ed.; Academic: New York, 1981; Vol. 6B, pp 1−77.

(24) Schatz, G. C.; Kuppermann, A. *J. Chem. Phys*. **1976**, *65*, 4642. Schatz, G. C.; Hubbard, L. M.; Dardi, P. S.; Miller, W. H. *J. Chem. Phys*. **1984**, *81*, 231.

(25) Sun, Q.; Bowman, J. M.; Schatz, G. C.; Sharp, J. R.; Connor, J. N. L. *J. Chem. Phys*. **1990**, *92*, 1677. Colton, M. C.; Schatz, G. C. *Int. J. Chem. Kinet*. **1986**, *18*, 961.

(26) Schatz, G. C. *Chem. Phys. Lett*. **1988**, *151*, 409. Schatz, G. C.; Sokolovski, D.; Connor, J. N. L. *J. Chem. Phys*. **1991**, *94*, 4311. Jakubetz, W.; Sokolovski, D.; Connor, J. N. L.; Schatz, G. C. *J. Chem. Phys*. **1992**, *97*, 6451. Connor, J. N. L.; McCabe, P.; Sokolovski, D.; Schatz, G. C. *Chem. Phys. Lett*. **1993**, *206*, 119. Sokolovski, D.; Connor, J. N. L.; Schatz, G. C. *Chem. Phys. Lett*. **1995**, *238*, 127; *J. Chem. Phys*. **1995**, *103*, 5979; *Chem. Phys*. **1996**, *207*, 461. Schatz, G. C.; Sokolovski, D.; Connor, J. N. L. In *Advances in Molecular Vibrations and Collision Dynamics*; Bowman, J. M., Ed.; JAI Press: Greenwich, CT, 1994; Vol 2B, pp 1−26.

(27) Bondi, D. K.; Connor, J. N. L.; Manz, J.; Römelt, J. *Mol. Phys*. **1983**, *50*, 467.